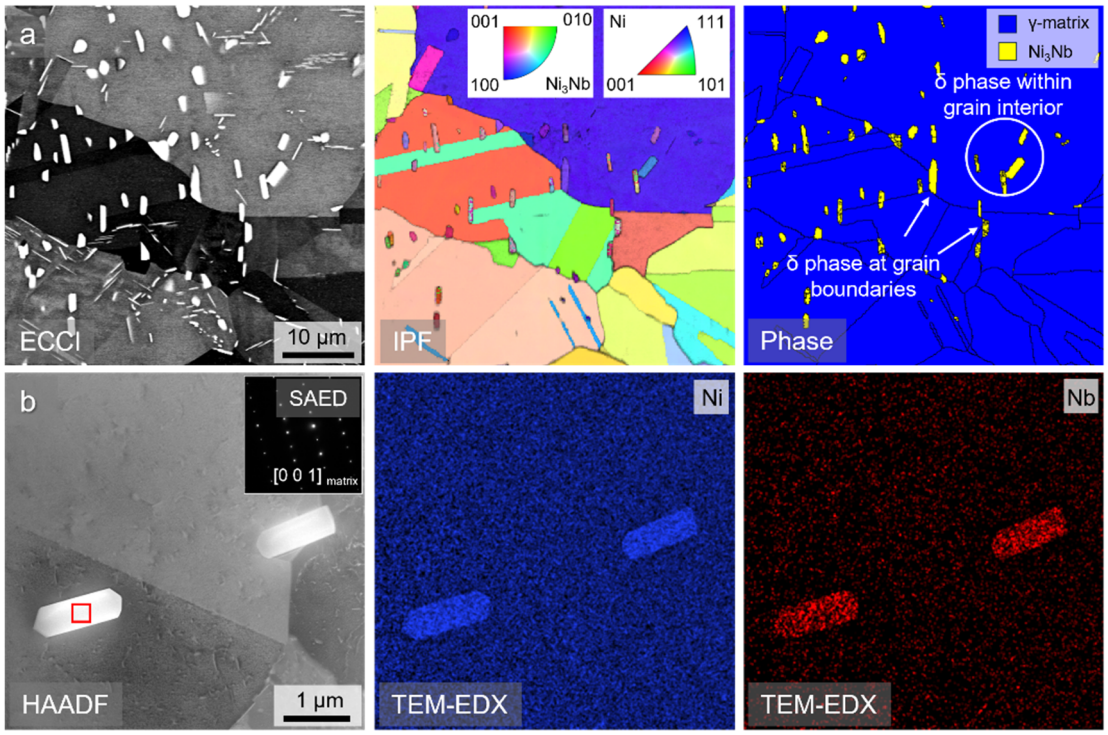

Extended Data Fig. 1 | Distribution, morphology and structure of the δ phase within the studied material IN718. a, Electron channeling contrast imaging (ECCI), electron backscatter diffraction (EBSD) inverse pole figure (IPF) and phase map, showing the distribution of the δ phase. **b**, High-angle annular dark-field scanning transmission electron microscopy (HAADF-STEM) image, showing the morphology of the δ phase. The selected area electron diffraction (SAED) pattern taken from the marked rectangular frame is placed as the inset to reveal the crystal structure ($D0_a$) of the δ phase. The corresponding energy-dispersive X-ray spectroscopy (EDX) maps of Ni and Nb are placed on the right-hand side.

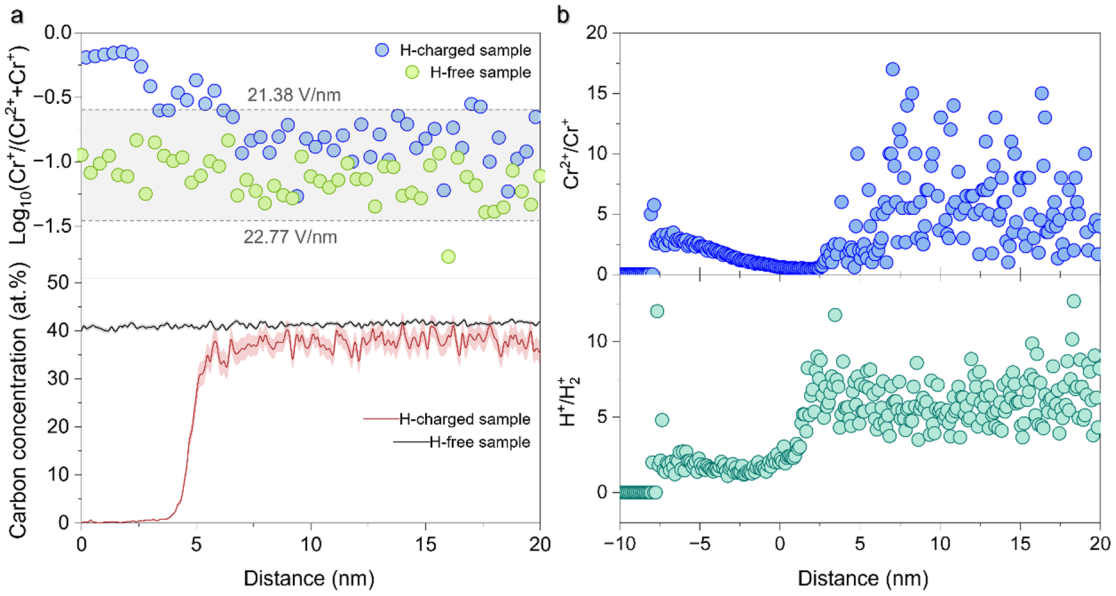

Extended Data Fig. 2 | The local electrical field analysis of regions close to carbide-matrix interfaces in APT specimens. a, Carbon (C) detection. The relative abundance of singly and doubly charged Cr ions plotted logarithmically within the APT specimens taken from bulk samples before and after *in situ* tensile testing under 2 MPa H_2 at 400 ˚C. Green circles represent hydrogen (H)-free sample (data also shown in Fig. 2c, in the manuscript, the initial state devoid of any charging or deformation); blue circles represent *in situ* H-charged sample (data also shown in Fig. 4g, in the manuscript, the state after H_2 exposure and simultaneous mechanical loading at 400 ˚C). Dash lines represent the upper and lower bounds of the charge-state ratio, $\mathrm{Log}_{10}^{Cr^+/(Cr^{2+}+Cr^+)}$. The corresponding electric fields are 21.38 V/nm and 22.77 V/nm, respectively. The respective C concentrations within individual carbides are accordingly plotted, suggesting a reduction in C concentration after *in situ* tensile testing under 2 MPa H_2 at 400 ˚C. The black line indicates H-free sample and red line indicate *in situ* H-charged sample. **b**, H detection. A notably higher ratios of Cr^{2+}/Cr^+ and H^+/H_2^+ is observed (data also shown in Fig. 4f and Fig. 4g, in the manuscript), despite the localized fluctuations, indicating a relatively high electric field in this carbide phase and vice versa in the FCC matrix. This suggests that the detected H originates intrinsically from the material, rather than external contamination.

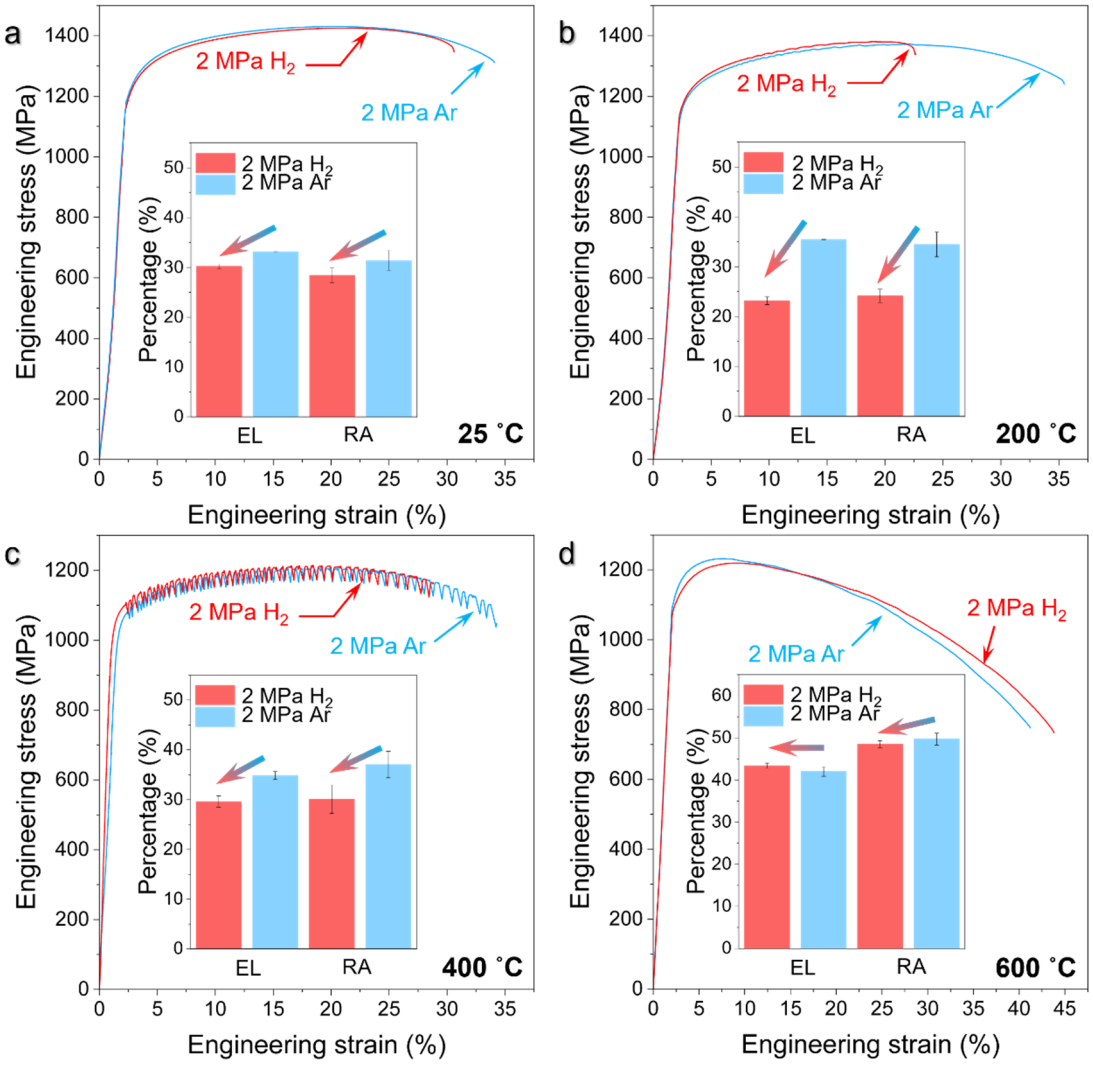

Extended Data Fig. 3 | Tensile stress-strain curves of the material loaded under 2 MPa H_2 and Ar at the strain rate of ~2.9 × 10^{-5} s^{-1}. a, 25 ˚C. **b**, 200 ˚C. **c**, 400 ˚C. **d**, 600 ˚C. The curves obtained in Ar atmosphere serve as references to reveal the occurrence of H-induced damage and its degradation effect on material's property, the total elongation (EL) and reduction in cross-sectional area (RA) values of samples loaded under 2 MPa H_2 and Ar are inset in each figure. At low temperatures (25 ˚C and 200 ˚C, corresponding to the temperature regime I as indicated in Fig. 1d), H embrittlement is primarily governed by H-enhanced decohesion (HEDE)[17,18] and/or H-enhanced localized plasticity (HELP)[19,20] or adsorption-induced dislocation emission (AIDE)[2]. Compared to 25 ˚C, a more severe reduction in EL and RA was observed at 200 ˚C, attributed to the higher H trapping rate (as illustrated in Fig. 1d of the manuscript). At higher temperatures (e.g., 400 ˚C), the dominant mechanism shifts to H-related chemical reaction with carbides. No H-induced degradation effect is observed at 600 ˚C, as the methane formation becomes thermodynamically unfavorable (as supported by DFT calculations in Fig. 5d of the manuscript).

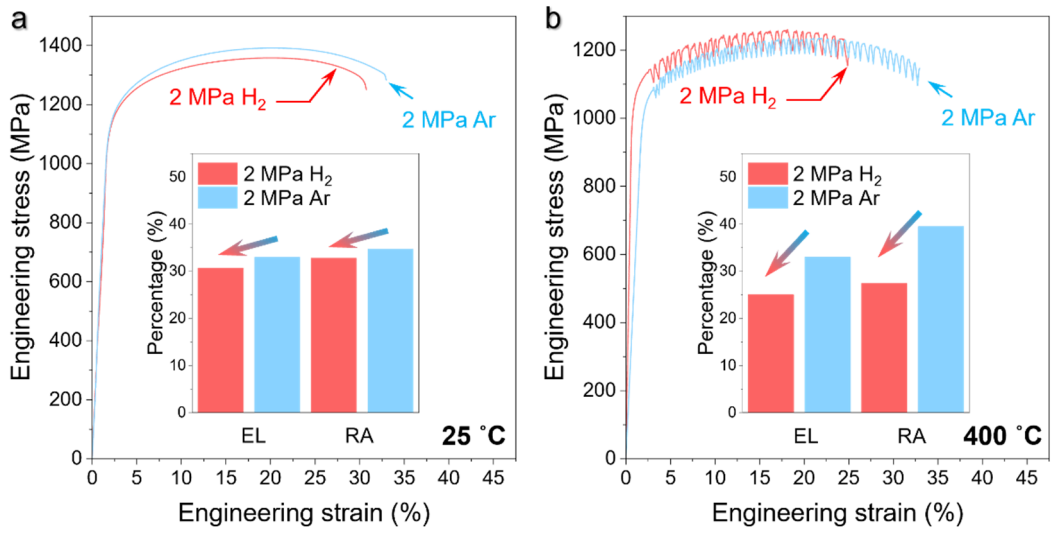

Extended Data Fig. 4 | Tensile stress-strain curves of the material loaded under 2 MPa H_2 and Ar at a lower strain rate of ~1.3×10^{-5} s^{-1}. a, 25 ˚C. **b**, 400 ˚C. Comparison to the data in Extended Data Fig. 3 shows that a slower strain rate has little effect on room-temperature H embrittlement, but induces a markedly stronger H embrittlement effect at 400 ˚C (24.1% of EL reduction at this temperature vs. 6.8% of EL reduction at room temperature).

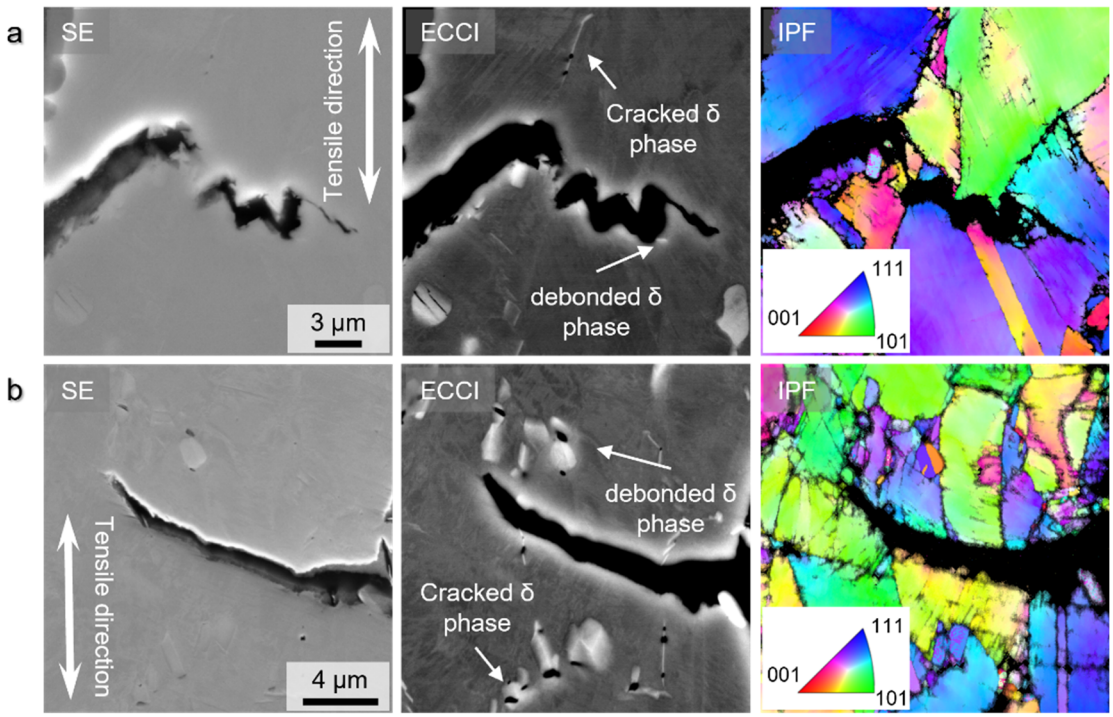

Extended Data Fig. 5 | H-induced damage behavior. a, 25 ˚C. **b**, 200 ˚C. The second electron (SE) images show the representative crack morphology and damage behavior observed after *in situ* tensile testing under H exposure. Corresponding ECCI and EBSD-IPF maps reveal that damages are formed within the δ phase or at the δ/γ interfaces, which promotes the formation and propagation of intergranular and transgranular cracks (corresponding to the damage mechanisms in the temperature regime I as indicated in Fig. 1d). Compared with 25 ˚C, an exacerbated H-induced damage associated with δ phase is observed at 200 ˚C, due to higher H trapping rate (as described in Fig. 1d).

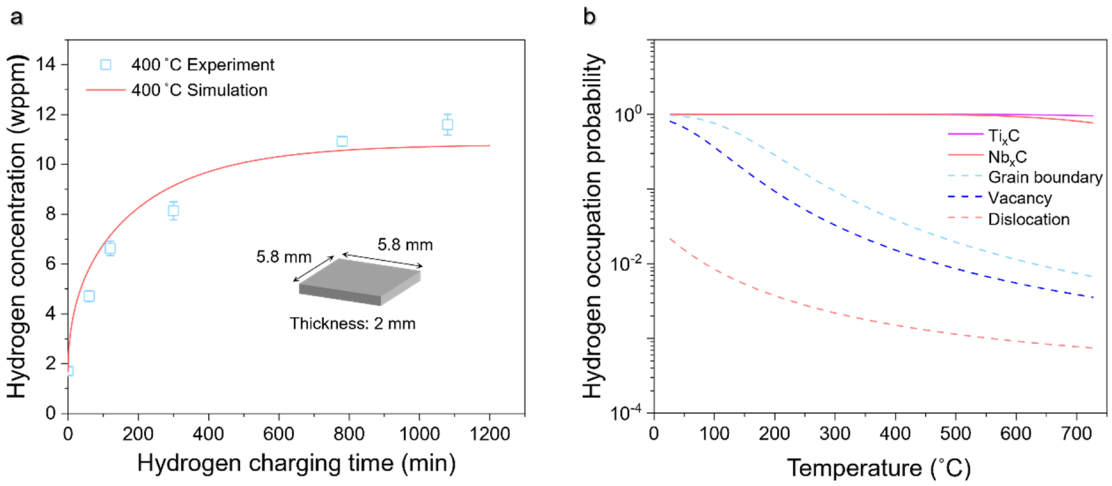

Extended Data Fig. 6 | H concentration and temperature dependence of H occupation probabilities at various defects. a, Experimentally measured H concentration at 400 ˚C for varying charging times (0, 60, 120, 300, 780 and 1080 min) and the corresponding diffusion analysis, with H-charging sample geometry inset. Post-charging samples were immediately quenched in liquid nitrogen following atmosphere venting. The H concentration was measured by hot extraction using a LECO ONH836 analyzer (calibrated using steel pin standards containing 6.9 wppm diffusible H). H diffusion and solubility coefficients were derived by fitting numerical simulations (performed using COMSOL Multiphysics software) to the experimentally measured H concentration data via minimizing the sum of squared errors. The calculated bulk H concentration (c_0) for ~0.5 h of charging was determined to be 4.8 wppm (weight parts per million). Activation energy for diffusion (Q_1 = −48.63 kJ/mol) and solution (Q_2 = −11.67 kJ/mol) were implemented in the numerical model[62]. The pre-exponential factors were determined to be D_0 = 1.26 × 10^{-7} m^2/s for diffusion and S_0 = 24 $mol/m^3 \cdot MPa^{1/2}$ for solubility, respectively. **b**, The occupation probability P_i of H at defect site i is calculated using the relation $P_i=1/[1+exp(-E_b^i/k_BT)/c_0]$, where c_0 = 4.8 wppm, E_b^i denotes the maximum H binding energies at each defect type, k_B is the Boltzmann constant and T is the temperature. Values of E_b^i for grain boundaries, vacancies, and dislocations are adopted from Ref. 11-13.

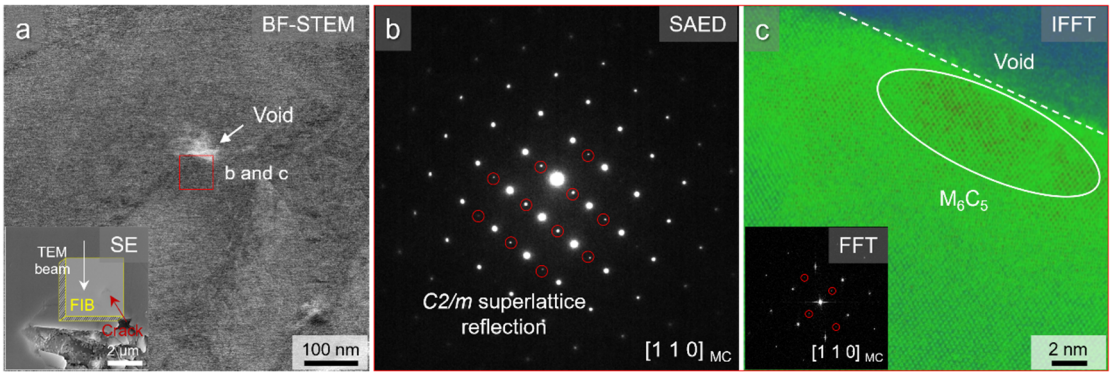

Extended Data Fig. 7 | Another transmission electron microscopy (TEM) analysis of regions close to carbide-matrix interface that are damaged upon mechanical loading and H_2 exposure at 400 °C. a, The overview bright-field scanning TEM (BF-STEM) image of a cracked carbide-matrix interface, with a SE inset showing the corresponding FIB-lifted area. **b**, Selected area electron diffraction (SAED) pattern taken from the rectangular frame in **a**, showing again superlattice spots that correspond well to the vacancy-ordered M_6C_5-type carbide (*C2/m* space group). (C) Inversed Fast Fourier Transformation (IFFT) image based on the superlattice reflection spots marked in the inset Fast Fourier Transformation (FFT) image taken from the rectangular frame in **a**, revealing the formation of M_6C_5-type carbide close to the carbide-matrix interfacial void. A probe current (*Ip*) of ~7 pA for BF-STEM and SAED imaging and of 3 pA for HAADF-STEM imaging were used to prevent any possible electron beam damage to the beam-sensitive newly formed carbide.

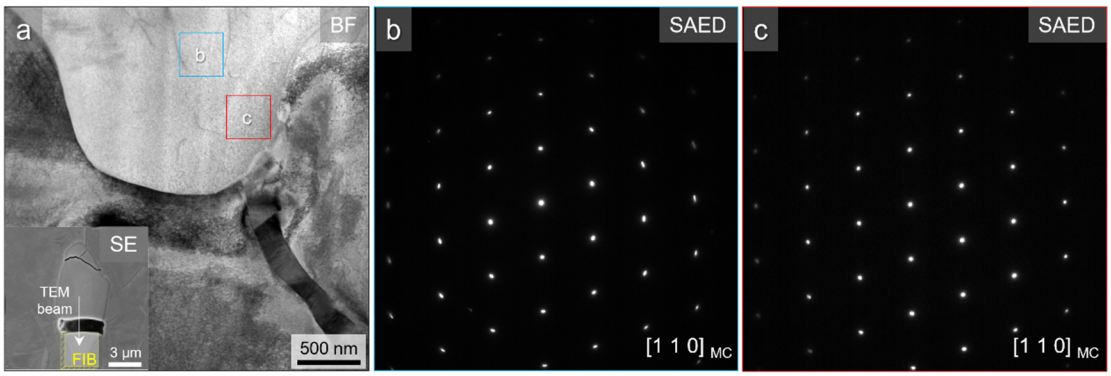

Extended Data Fig. 8 | TEM analysis of regions close to carbide-matrix interface after mechanical loading under Ar atmosphere at 400 ˚C. a, The overview TEM bright field (BF) image, with a SE inset showing the corresponding FIB-lifted area. **b**.**c**, SAED patterns acquired from regions indicated by the blue and red rectangle frame marked in **a**, respectively. The MC carbide maintains its initial FCC (B1) structure with no superlattice structure observed.

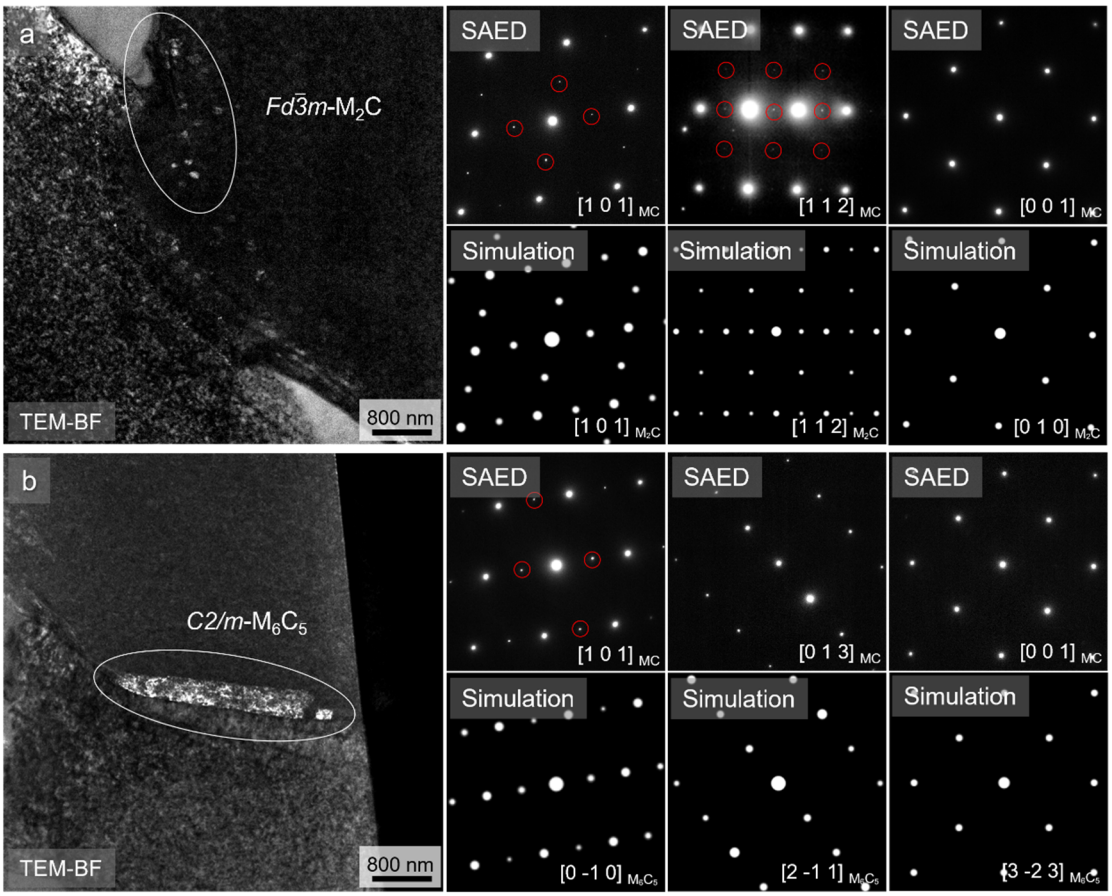

Extended Data Fig. 9 | TEM dark-field (DF) image, experimental and simulated SAED patterns for carbide phases. a, M_2C. **b**, M_6C_5. Experimental SAED patterns were acquired from various zone axes and compared with simulations performed using CrysTBox software[63], the red circles mark the superlattice diffraction spots corresponding to the DF images.

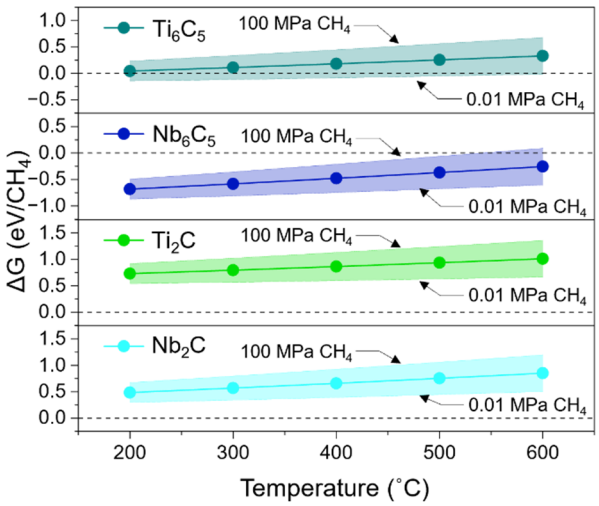

Extended Data Fig. 10 | Thermodynamics of H-carbide interaction without H uptake in C vacancies within carbides. Gibbs free energy change (ΔG) for the H-induced formation of CH_4 and vacancy-ordered carbides without H occupation, calculated at a fixed H_2 partial pressure of 2 MPa and varying CH_4 pressures (the point-line represents 1 MPa CH_4, shaded zone represents 0.01–100 MPa CH_4). The ΔG was evaluated considering the reaction: $2(1-x) + MC \rightarrow MC_x + (1-x)CH_4$. This reaction is thermodynamically less favorable ($\Delta G > 0$ for most modelling scenarios) in the absence of H uptake in C vacancies, compared to the DFT calculations shown in Fig. 5d of the manuscript.

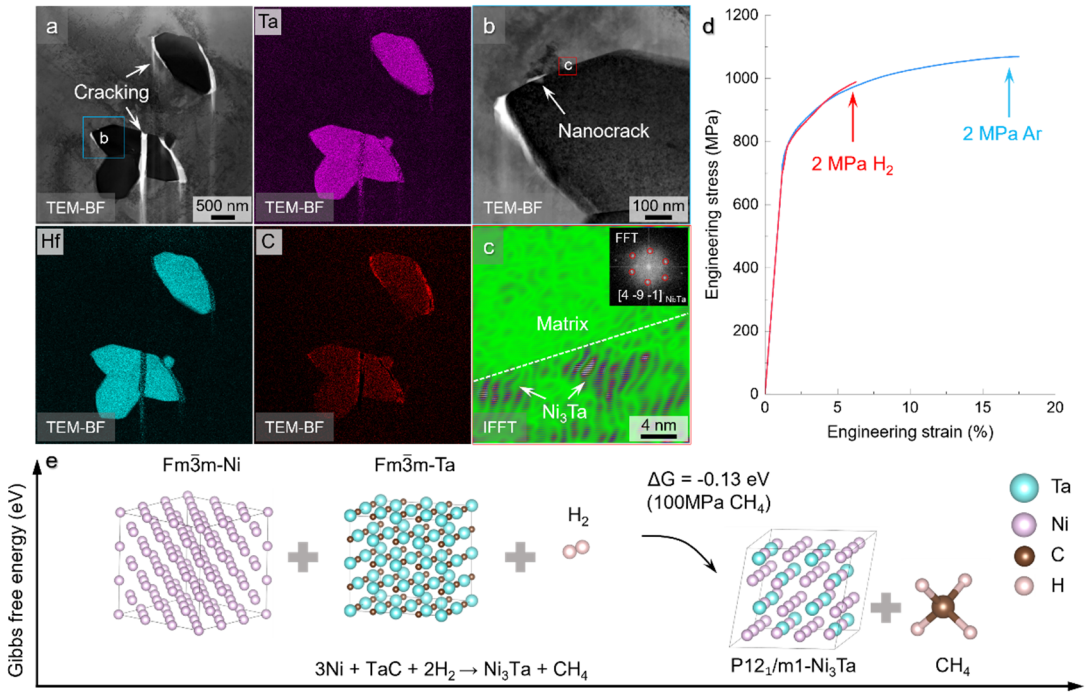

Extended Data Fig. 11 | H-induced damage behavior for directionally solidified CM247LC Ni-based alloy and DFT calculation of H-carbide interaction at 600 ˚C. a, The overview TEM-BF image and the corresponding TEM-EDX mapping of cracked (Ta,Hf)C carbides of the sample failed in H atmosphere. **b**, TEM-BF image taken from the blue rectangle frame marked in **a**, showing the cracked carbide-matrix interface and an adjacent nanocrack. **c**, IFFT image based on the reflection spots marked in the inset FFT image, which is taken from the red rectangle frame marked in **b**, suggesting the formation of Ni_3Ta phase (*P12₁/m1* space group) due to the presence of H. **d**, Tensile stress-strain curves of the material loaded under 2 MPa H_2 and Ar at 600 ˚C. The H-induced degradation in tensile elongation is due to the facile carbide debonding induced by H and the associated reactions. **e,** Thermodynamic feasibility of the chemical reaction shown in the figure at 600 ˚C with 2 MPa H_2 and 100 MPa CH_4. The Gibbs free energy calculation (using the same procedures and DFT parameters in the main text) shows that this reaction is favorable at 600 ˚C. These findings demonstrate that the proposed high-temperature H embrittlement mechanism can be applied to other alloys, independent of carbide type or temperature regime.